ELSEVIER

Global and Planetary Change 33 (2002) 139–153

GLOBAL AND PLANETARY CHANGE

www.elsevier.com/locate/gloplacha

Modelled glacial and non-glacial HCO_3^-, Si and Ge fluxes since the LGM: little potential for impact on atmospheric CO_2 concentrations and a potential proxy of continental chemical erosion, the marine Ge/Si ratio

I.W. Jones [a], G. Munhoven [a,b], M. Tranter [a,*], P. Huybrechts [c], M.J. Sharp [d]

[a] *Bristol Glaciology Centre, School of Geographical Sciences, University of Bristol, Bristol, BS8 1SS, UK*
[b] *Laboratoire de Physique Atmosphérique et Planétaire, Université de Liège, 5 avenue de Cointe, B-4000 Liège, Belgium*
[c] *Vrije Universiteit Brussel, Department Geografie, Pleinlaan 2, B-1050 Brussels, Belgium*
[d] *Earth and Atmospheric Sciences, University of Alberta, Edmonton, Alberta, Canada T6G 2E3*

Received 19 April 2000; received in revised form 3 April 2001; accepted 3 July 2001

Abstract

The runoff and riverine fluxes of HCO_3^-, Si and Ge that arise from chemical erosion in non-glaciated terrain, are modelled at six time steps from the Last Glacial Maximum (LGM) to the present day. The fluxes that arise from the Great Ice Sheets are also modelled. Terrestrial HCO_3^- fluxes decrease during deglaciation, largely because of the reduction in the area of the continental shelves as sea level rises. The HCO_3^- fluxes, and the inferred consumption of atmospheric CO_2 are used as inputs to a carbon cycle model that estimates their impact on atmospheric CO_2 concentrations ($^{atms}CO_2$). A maximum perturbation of $^{atms}CO_2$ by $\sim$ 5.5 ppm is calculated. The impact of solutes from glaciated terrain is small in comparison to those from non-glaciated terrain. Little variation in terrestrial Si and Ge fluxes is calculated ($<10\%$). However, the global average riverine Ge/Si ratio may be significantly perturbed if the glacial Ge/Si ratio is high. At present, variations in terrestrial chemical erosion appear to have only a reduced impact on $^{atms}CO_2$, and only little influence on the global Si and Ge cycle and marine Ge/Si ratios during deglaciation.

Keywords: HCO_3^-, Si and Ge fluxes; LGM; atmospheric CO_2 concentration; marine Ge/Si ratio

1. Introduction

The atmospheric concentration of CO_2, $^{atms}CO_2$, is believed to be one of the important factors which moderates the response of global mean temperature to Milankovich forcing (Petit et al., 1999). This is because the variation in the concentration of CO_2 in air bubbles in the Vostok ice core, which is commonly used as a proxy for temporal variations in $^{atms}CO_2$ over the last 300–400 ka, shows a positive association with air temperature variations derived from the $\delta^{18}O$ and δD contents of the ice. The $^{atms}CO_2$ at the last glacial maximum (LGM), about 21 ka BP, was $\sim$ 195 ppm, while the pre-industrial value for the current interglacial is $\sim$ 280 ppm. The difference in concen-

* Corresponding author. Tel.: +44-117-928-8307; fax: +44-117-928-7878.
E-mail address: M.Tranter@bristol.ac.uk (M. Tranter).

0921-8181/02/$ - see front matter
PII: S0921-8181(02)00067-X

trations is 85 ppm. Only a few of the major processes which lead to variations of $^{atms}CO_2$ from the LGM to the present have been quantified to date. The decrease in salinity of the oceans during the deglaciation was responsible for a $^{atms}CO_2$ decrease by ~11 ppm (Broecker, 1995). The terrestrial organic carbon reservoir is thought to have increased by 270–720 Gt C (Bird et al., 1994). It is estimated that ultimately ~15% of this amount (1/6.5 or about 40–110 Gt C) came from the atmospheric and 85% from the oceanic carbon reservoirs (Siegenthaler, 1993). As a result, the increase of the biospheric carbon reservoir would have led to a decrease in $^{atms}CO_2$ of ~19–52 ppm. However, due to the response of carbonate compensation in the ocean, the actual decrease on $^{atms}CO_2$ after several thousand years is about a factor of two lower (Siegenthaler, 1993), and would thus only be 9–26 ppm. The global average surface ocean temperature increased by 2–5 °C during the deglaciation, leading to an increase in $^{atms}CO_2$ of 22–52 ppm (Broecker, 1995). Hence, a net variation of 8.5 ± 17 ppm can be explained (assuming that the different uncertainties are independent of each other and thus add quadratically). The best estimate increase of 8.5 ppm represents only 10% of that recorded in the Vostok ice core. To date, there is no consensus on the processes that are responsible for the generation of the remaining 90%. The search for the processes that could help to explain the rest of the observed 85 ppm focuses on a possible decrease in the effectiveness of the ocean's biological pump (Broecker, 1995), increased deposition of reef carbonates (Berger, 1982; Opdyke and Walker, 1992; Walker and Opdyke, 1995; Kleypas et al., 1999) and changes in deep ocean pH (Sanyal et al., 1995).

It is generally believed that changes in global chemical erosion rates are of insufficient magnitude to contribute to a change in $^{atms}CO_2$ on glacial–interglacial time scales (Broecker, 1995). A decrease in the chemical erosion of silicates during the deglaciation would lead to a decrease of $^{atms}CO_2$, but the decrease in chemical erosion rates that are necessary to perturb $^{atms}CO_2$ by more than a few ppm are relatively large (Munhoven and François, 1994, 1996). A decrease in the global rate of carbonate weathering during the deglaciation would also have led to an increase in $^{atms}CO_2$, due to changing carbonate compensation (Broecker, 1995). However, $^{atms}CO_2$ variations produced by carbonate weathering are only about half as important as those produced by silicate weathering, at a given consumption rate of atmospheric CO_2 (Munhoven and François, 1996). The transition from the LGM to the present was accompanied by changes in the quantity and distribution of runoff from glaciated and non-glaciated terrain and the drowning of shelf carbonate exposures by rising sea level (Opdyke and Walker, 1992; Gibbs and Kump, 1994; Kump and Alley, 1994). These factors impact on the rate of global chemical erosion, but to date their quantitative impact on $^{atms}CO_2$ is only poorly constrained. Gibbs and Kump (1994) were the first to quantify the global distribution of runoff at the LGM and the present, and to use transfer functions based on lithology to convert runoff into fluxes of HCO_3^-, which were higher at the LGM. A major unknown in their study was the flux of runoff and solutes from ice sheets. However, the theoretical sensitivity tests carried out by Gibbs and Kump (1994) suggested that changes in the global terrestrial fluxes of HCO_3^- were capable of changing $^{atms}CO_2$ if there was significant chemical erosion in ice marginal areas.

In this paper, we extend the analysis and approach proposed by Gibbs and Kump (1994). Additional time steps during deglaciation are analysed and a better definition of the magnitude of glacial runoff and glacial chemical erosion is used. Finally, a more detailed ocean carbon cycle model, allowing time-dependent simulation experiments, is used to quantify the impact of the variations of the terrestrial fluxes during the deglaciation on $^{atms}CO_2$.

We also examine the likely perturbation of terrestrial Ge and Si fluxes and their impact on marine Ge/Si ratios, since this is an area of current controversy. Ge/Si ratios within opals derived from deep ocean cores (Mortlock et al., 1991) vary on glacial to interglacial time scales. Froelich et al. (1992) and Bareille et al. (1998) have shown that these ratios within the opal faithfully record those of the ocean at the time they were formed. Primary controls on Ge/Si ratios within the oceans may include terrestrial chemical weathering intensity (Froelich et al., 1992), but more recent work suggests that diagenetic effects (Hammond et al. 2000; King et al., 2000) and the preferential weathering of minerals with high Ge/Si ratios, particularly biotite (Filippelli et al., 2000), are

probably more important. Murnane and Stallard (1990) argue that the Ge/Si ratio of riverine solute [$(Ge/Si)_{riv}$] is lower than that of the underlying bedrock due to the preferential retention of Ge in secondary mineral phases (e.g. clays). The amount of Ge retained within clays is dependent on weathering intensity: the lower the weathering intensity, the higher the Ge/Si ratio in the secondary mineral phases, and consequently, the lower the Ge/Si ratio in the riverine water. Froelich et al. (1992) suggested that the variations in $(Ge/Si)_{seawater}$ are driven by large glacial to interglacial changes in continental weathering intensity, resulting in a two-fold increase in the amount of dissolved silica and a 20% reduction in the $(Ge/Si)_{riv}$ ratio. Chillrud et al. (1994) have published the only glacial meltwater Ge/Si ratio to date. A maximum ratio of 1.35 pmol/μmol is given, which is more than double that of the global average riverine Ge/Si of 0.6 pmol/μmol (Froelich et al., 1992). With an increase in the runoff of glacial meltwater during the main period of deglaciation (7–12 ka BP), there is a possibility that these higher ratios would increase the corresponding ratios within the oceans. The following modelling approach will explore this possibility quantitatively.

2. Methodology

Both non-glacial and glacial terrestrial chemical erosion were modelled over the last deglaciation in order to calculate the potential change in $^{atms}CO_2$ that arises from variations in terrestrial chemical erosion. Non-glacial fluxes of HCO_3^-, Si and Ge, dependant on runoff and lithology were simulated using a methodology adapted from Gibbs and Kump (1994) for five periods during the last deglaciation (6, 11, 14, 16, and 21 ka BP). Glacial fluxes of HCO_3^-, Si and Ge were determined from 21 ka BP to the present on the basis of meltwater fluxes derived from a thermo-mechanically coupled model of ice-sheet growth and decay in the Northern Hemisphere (Huybrechts and T'siobbel, 1997) and using an estimation of the likely chemical composition of the glacial runoff (Jones et al., 1999; Tranter et al., in preparation). The calculated HCO_3^- production and in $^{atms}CO_2$ consumption fluxes were used as inputs to a model of the ocean carbon cycle (Munhoven and François, 1996; Munhoven, 1997) to determine the corresponding change in $^{atms}CO_2$. The definition of global land area and lithology during deglaciation is described first, followed by descriptions of the calculation of the non-glacial and glacial fluxes and the estimation of their impact on $^{atms}CO_2$.

2.1. Land area grid

The global land area mask is a $1 \times 1^\circ$ grid derived from Gibbs and Kump (1994), which includes the exposure of the continental shelves at the LGM. The ice sheet extent at 6, 11, 14, 16 and 21 ka BP was derived from Peltier (1994), as was the shelf exposure.

2.2. Global lithology

The original $2 \times 2^\circ$ map of terrestrial lithology used by Gibbs and Kump (1994) was downscaled to a $1 \times 1^\circ$ resolution in order to map onto the land area and the runoff grids described below. The lithology grid includes areas of exposed continental shelf at the LGM (but does not include bedrock that is presently covered by ice masses, mainly in Antarctica and Greenland, which is not relevant for the modelling undertaken here). The map considers six different lithological classes of rock types exposed (Table 1), namely carbonate, shale, sandstone, extrusive igneous, shield and complex. The "complex" lithology covers 26.5% of the landmass (excluding exposed shelves). Each grid cell of complex lithology was assigned a composition in terms of the other five

Table 1
The present-day exposed lithology at the earth surface

Rock type	Global lithology map	Amiotte Suchet (1995)	Calculated composition of 'complex' lithology cells	
	%Area	%Area	%Area	%Area of 'complex'
'Complex'	26.5	N/A		
Carbonate	10.0	14.0	4.0	15.1
Shale	12.4	25.0	12.6	47.5
Sandstone	24.8	26.0	1.2	4.6
Extrusive igneous	6.4	8.0	1.6	5.9
Shield	19.9	27.0	7.1	26.9
Totals	100.0	100.0	26.5	100.0

primary lithological classes, such that the global average lithological distribution matched that of Amiotte Suchet (1995). Hence, each complex grid cell contains 15%, 48%, 4.6%, 5.9% and 27% of carbonate, shale, sandstone, extrusive igneous and shield rocks, respectively (Table 1).

2.3. Exoreic runoff fluxes: non-glacial and glacial

Climatologies from simulation experiments carried out with the NCAR CCM1 General Circulation Model (GCM) were used to provide the distributions of non-glacial runoff (Kutzbach et al., 1996, 1998) at 21, 16, 14, 11 and 6 ka BP, and at the present day (control run). CCM1 uses a $4.5 \times 7.5^\circ$ global grid. The results were downscaled to $1 \times 1^\circ$ using an area-weighted redistribution procedure. The GCM-based runoff distributions were only used to estimate runoff differences (anomalies) between each of the five time slices during deglaciation and the present day. Anomalies $\Delta R(t)$ for each grid cell at each time slice t are obtained by subtracting the present-day value R_{GCM}(present) given by the control-run experiment from the value $R_{\mathrm{GCM}}(t)$ at t, i.e., $\Delta R(t) = R_{\mathrm{GCM}}(t) - R_{\mathrm{GCM}}(\mathrm{present})$, $t = 21$, 16, 14, 11 and 6 ka BP. The absolute runoff values $R(t)$ actually used for the calculations in the model at each time slice t were derived by adding the estimated anomalies $\Delta R(t)$ to the observed present-day distribution R_{obs}(present), taken from Cogley (1998), which is 44,800 $\mathrm{km}^3\ \mathrm{year}^{-1}$: $R(t) = R_{\mathrm{obs}}(\mathrm{present}) + \Delta R(t)$. This commonly adopted method is meant to minimise the impact of possible systematic biases in the GCM results, which should cancel out in this procedure. The global exoreic runoff volume to the oceans for each time slice t was calculated as the sum of the absolute values in grid cells that lie within the limits of externally drained basins.

Results from a three-dimensional thermomechanically coupled model of ice-sheet growth and decay in the Northern Hemisphere (Huybrechts and T'siobbel, 1995) were used to estimate glacial runoff over the last 21 ka (Fig. 1). The model has been tested against, and found to be consistent with, the Greenland and Antarctic ice sheets (Huybrechts, 1990; Huybrechts et al., 1991). The main inputs to the ice-sheet model are bed topography, mean annual surface temperature and the mass balance. The inputs to the mass-balance model are data sets for present-day mean monthly sea-level

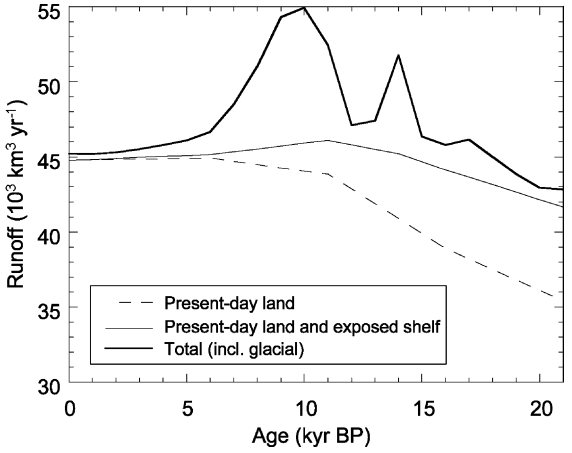

Fig. 1. Global, exoreic runoff during the last deglaciation, showing non-glacial continental runoff (excluding continental shelves), non-glacial continental runoff including continental shelves and total runoff (including meltwater from the Great Ice Sheets).

air temperature and mean monthly precipitation rates obtained from standard climatologies, which are perturbed in different environments to take into account the effects of ice-sheet elevation, atmospheric temperature change and the moisture-holding capacity of the overlying column of air. The mass-balance model distinguishes between snow accumulation and runoff and is driven by a temperature record over the last 130 ka derived from the GRIP ice core (Dansgaard et al., 1993). Following procedures successfully adopted for the Greenland ice sheet (Reeh, 1989), the melting rate is set proportional to the yearly sum of positive-degree days at the ice-sheet surface, and the final amount of runoff is obtained as the sum of meltwater that does not refreeze in the snowpack and of any water resulting from basal melting. It has been shown that this ice-sheet model is able to reproduce the growth and decay of the Northern Hemisphere ice sheets in good accordance with glacial–geological data (Huybrechts and T'siobbel, 1997).

Runoff (excluding ice calving) from the Laurentide, Cordilleran, Fennoscandian, Kara, Barents and Greenland ice sheets was calculated, but runoff from Southern Hemisphere ice masses, such as in Patagonia, is excluded. Runoff from the Antarctic ice sheet is believed to be trivial compared to the fluxes calculated here (Huybrechts and Oerlemans, 1990; Jacobs et al., 1992).

2.4. Reconstructing HCO_3^-, Si and Ge fluxes over the last deglaciation

The modelling approach of Gibbs and Kump (1994) was extended and adapted to calculate the distribution of global non-glacial riverine HCO_3^- and Si fluxes during the last deglaciation. Empirical relationships relate HCO_3^- and Si yields to runoff intensity for the five different rock classes (Bluth and Kump, 1994). Hence, for each grid cell that gives rise to exoreic runoff, the absolute runoff is converted into a HCO_3^- and Si yield dependant on lithology. The global flux for each time step is the sum of the yields in each grid cell. Non-glacial germanium fluxes were derived using the following equation, derived from Froelich et al. (1992):

$$[\mathrm{Ge}](\mathrm{pM}) = 0.33\ [\mathrm{Si}](\mu M) + 38 \quad (1)$$

where [Ge] and [Si] are the riverine Ge and Si concentrations. Eq. (1) is used to calculate the Ge concentration in the runoff in each grid cell contributing to the exoreic runoff in non-glaciated areas. The Ge flux to the ocean contributed by each grid cell can thus directly be derived from the corresponding Si flux and the runoff volume.

Glacial fluxes of HCO_3^-, Si and Ge were obtained as follows. Glacial runoff fluxes were multiplied by the current best average glacial meltwater HCO_3^- and Si concentrations (309.7 and 5.9 μmol/l, respectively; Tranter et al., in preparation) to give glacial meltwater fluxes of Si and HCO_3^-. This method gives a conservative estimate of HCO_3^- fluxes, since the average glacial HCO_3^- concentration is derived from non-carbonate bedrock, and chemical weathering in the proglacial zone and dissolution of suspended sediment is ignored. The potential for chemical weathering of glaciogenic sediment in proglacial environments also suggests that our estimate of the glacial Si flux is also conservative. Chillrud et al. (1994) derived the Ge/Si ratio of a glacial meltwater stream of the Argentine Andes mountains, and found that these data agree well with those of global river data (Mortlock and Froelich, 1987). The highest Ge/Si ratio (1.35 pmol/μmol) measured by Chillrud et al. (1994) derives from a water sample which had a Si concentration of ~ 36 μmol/l (see also Froelich et al., 1992). On the basis of the regression line given by Froelich et al. (1992) for the meltwater stream studied by Chillrud et al. (1994), a glacial Ge/Si ratio of 6.6 pmol/μmol is calculated for a Si concentration of 5.9 μmol/l. This glacial Ge/Si ratio is used to derive the glacial Ge flux from the modelled Si flux and will give the best estimate of changes in the glacial Ge flux at the LGM and during the last deglaciation.

2.5. Global carbon cycle model

The ocean carbon cycle model described in Munhoven and François (1996) and Munhoven (1997) was used in this study to estimate the impact of the changes in the weathering fluxes on atmospheric CO_2. The model represents the ocean–atmosphere subsystem of the global carbon cycle as a set of eleven homogeneous reservoirs, one atmospheric and 10 (five surface, two intermediate and three deep) oceanic. reservoirs). The geometry of the oceanic reservoirs is based upon five realistic profiles of the sea-floor depth and changes as a function of the prescribed sea-level evolution. The model includes mass balance equations for dissolved inorganic carbon (DIC), total alkalinity (TA), phosphate (chosen as the limiting nutrient) and oxygen in the 10 oceanic reservoirs, $^{atms}CO_2$ in the atmospheric reservoir, and the $\delta^{13}C$ and $\Delta^{14}C$ isotopic characteristics in all of them. The mass balance equations include terms to represent the air–sea exchange of CO_2 and the transport of dissolved species by water circulation. Further taken into account is the production of organic and inorganic (carbonate) particles by biological activity in the surface reservoirs. Organic particles rain down to the intermediate and deep reservoirs where they are completely remineralised and their constituents released back to solution. A fully coupled model of the upper sediment column at eighty sea-floor depth levels for each of the five bathymetric profiles is then used to determine the ocean–sediment exchange of carbonate particles falling down to the sea floor from the surface regions. Depending on the degree of supersaturation with respect to calcite and aragonite at each depth level, carbonate particles may either dissolve, and their dissolution products diffuse back to the ocean, or accumulate and eventually buried into the deeper sediment. The required saturation depths are calculated from the concentrations of CO_3^{2-} in the deep reservoirs and the thermodynamic solubility products of calcite and aragonite. The sediment model generates vertical

sediment profiles and can therefore take chemical erosion of deep-sea sediments into account. A separate scheme is used to represent the carbonate accumulation in coral reefs and on banks and shelves in the coastal zone. Both fluxes vary as a function of sea level and of sea-level variation rate.

Finally, the mass balance equations also include terms to take into account the consumption of atmospheric CO_2 and the transfer of bicarbonate to the ocean due to continental weathering processes, as well as the supply of CO_2 to the ocean–atmosphere system by volcanic and hydrothermal activity. Scenarios for these fluxes need to be prescribed. We then use the model to calculate the impact of various chemical weathering scenarios on the evolution of the global distributions of dissolved inorganic carbon and of total alkalinity, and thus of CO_2 in the atmosphere and the concentration of CO_3^{2-} in the deep sea. This latter dynamically adjusts in such a way that the overall losses of dissolved inorganic carbon and of total alkalinity through carbonate burial in the seafloor sediments matches the transfer of carbon from the crust to the ocean–atmosphere and the supply of alkalinity and dissolved inorganic carbon by chemical weathering processes as closely as possible.

3. Results and discussion

3.1. Global runoff since the LGM

Runoff from the ice-free continents was ~ 9400 $km^3\ year^{-1}$ lower at the LGM than at present. However, runoff from the exposed continental shelf area (12.3×10^6 km^2) gave rise to an increase of about 6300 $km^3\ year^{-1}$, giving a net decrease of non-glacial runoff at the LGM of 3100 $km^3\ year^{-1}$ (Fig. 1). This 7% decrease in non-glacial runoff at the LGM is comparable with the 9% decrease calculated by Ludwig et al. (1999), who used a different methodology to that used here. It is a greater decrease than the 2% calculated by Gibbs and Kump (1994). This is due to the different GCM used here and the fact that their reported exposed continental shelf area of 15.9×10^6 km^2 could not be reproduced. The increase in total global runoff at the LGM due to the addition of glacial meltwater is 1200 $km^3\ year^{-1}$, which represents less than 3% of the total global runoff (Fig. 1). The reduction in exoreic, non-glacial runoff is in line with palaeoenvironmental investigations that suggest that the non-glaciated earth was drier at the LGM (Broecker, 1995).

The publicly available runoff data derived from CCM1 simulations have, for the first time, allowed the modelling of runoff during the last deglaciation. There is a net increase in non-glacial runoff from the LGM towards 11 ka BP, due mainly to the decrease in land covered by ice sheets (Fig. 1), leading to an increase of ca. 3% in the area of the non-glaciated continents. The contribution of exposed continental shelves to total non-glacial runoff over the last deglaciation was greatest at the LGM (15% of the total), in comparison with no effect for the present day (Fig. 1).

The global distribution of the change in non-glacial runoff is given in Fig. 2. The extent of ice sheets at the LGM (Peltier, 1994) have been masked out along with areas of internal drainage (Cogley, 1998). Areas with reduced runoff at the LGM include present-day South East China, large areas of Brazil and Peru, as well as immediately in front of the Eurasian Ice Sheet. Substantial increases in the runoff at the LGM derive from the exposed continental margins due to sea level fall, especially off the coast of present-day Indonesia.

The delivery of glacial runoff from the Great Ice Sheets over the last deglaciation occurs in three distinct phases, centred around 17, 14 and 10 ka BP (Fig. 3). The origin of the glacial runoff is distributed evenly around the margins of these ice sheets. The main period of increased glacial runoff is between 12 and 7 ka BP, coinciding with the main period of deglaciation (Petit et al., 1999). At the height of deglaciation, runoff of glacial meltwater was ~ 18% that of non-glacial runoff. At present, runoff from ice sheets (mainly Greenland) represents about 1% of total global runoff.

Total global runoff, which includes glacial meltwater, was only slightly lower at the LGM (net decrease of 2400 $km^3\ year^{-1}$) than at present. During the peak of glacial runoff (10 ka BP), total (glacial and non-glacial) global runoff was 22% higher than its present-day value. Although short lived events might have led to substantially higher glacial runoff volumes than those reported in Fig. 3, the magnitude or base level of global runoff is primarily governed by non-glacial runoff, while glacial runoff has a second order effect and controls patterning around the base level.

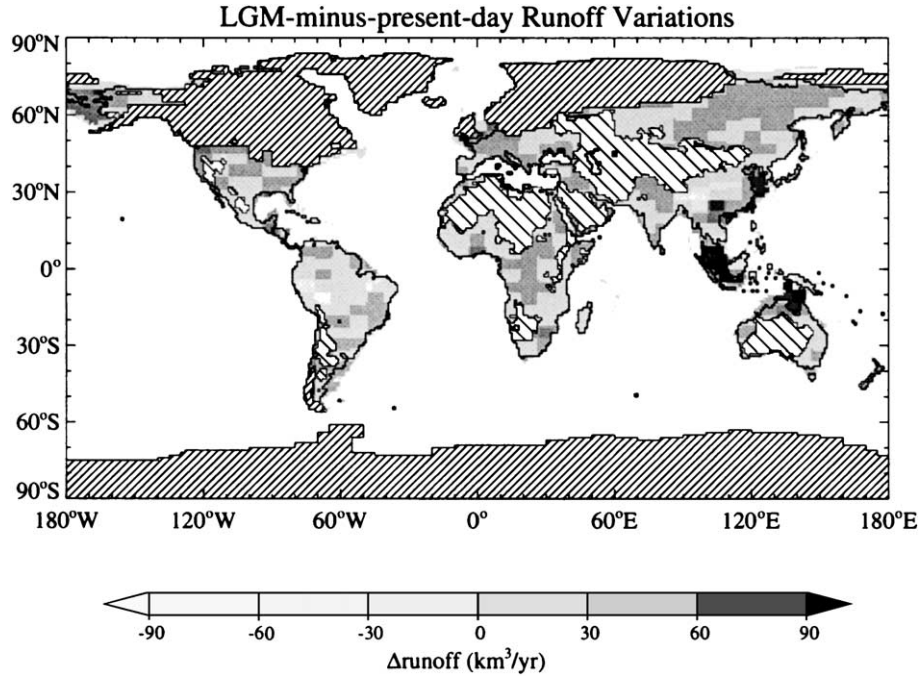

Fig. 2. Differences between the LGM and present-day global distributions of non-glacial runoff.

3.2. HCO_3^- fluxes

Non-glacial global HCO_3^- was 30.1 T mol year^{-1} at the LGM, rising to 30.6 T mol year^{-1} at 16 ka BP, some 26% higher than the modelled present-day value of 24.3 T mol year^{-1} (Fig. 4). These fluxes are almost certainly underestimates, since the best estimate of the present day HCO_3^- flux is 36.3 T mol HCO_3^- year^{-1} (Gaillardet et al., 1999). However, the relative changes in the fluxes between each time step are of greater importance in this study. Both LGM

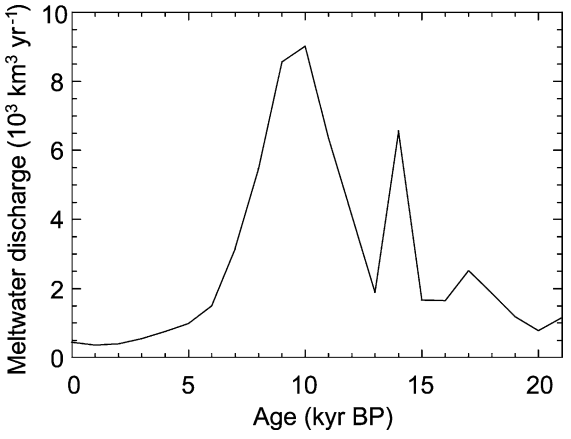

Fig. 3. Modelled glacial runoff for the last deglaciation (after Huybrechts and T'siobbel, 1995).

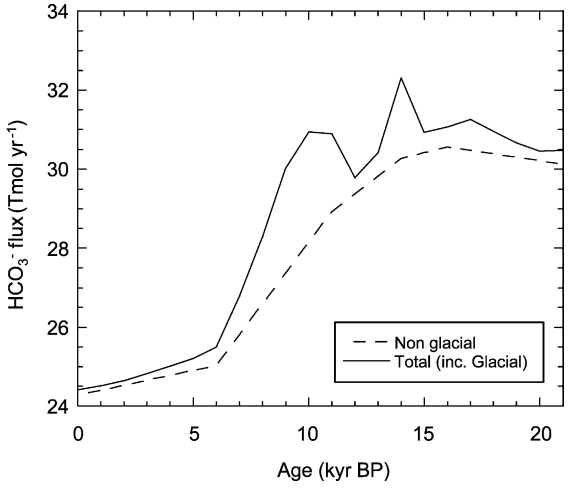

Fig. 4. Variation in the non-glacial and the total (non-glacial + glacial) terrestrial HCO_3^- flux during the last deglaciation.

and present-day results are in good accordance with those calculated by Gibbs and Kump (1994), who find that the non-glacial HCO_3^- flux was 5.1 T mol $year^{-1}$ higher at the LGM. It should, however, be emphasised that Gibbs and Kump (1994) used different data sets for the present-day runoff distribution and for the glacial–interglacial anomalies. While global non-glacial runoff has been steadily increasing since the LGM, non-glacial HCO_3^- fluxes have been decreasing, particularly during the main deglaciation period (16–6 ka BP). This sharp decrease is in line with an increase in sea level which results in a reduction of the exposed continental shelves (Table 2). There is a slight increase in the non-glacial HCO_3^- flux between the LGM and 16 ka BP, since the flux from the continents is increasing at a greater rate than the decrease observed on the exposed continental shelves (Tables 3 and 4).

The global distribution of non-glacial HCO_3^- change (Fig. 5) is broadly similar to that of runoff distribution. The greatest reduction in the HCO_3^- flux takes place in an area located to the east of the Tibetan Plateau. Here, the fluxes are reduced by as much as 2×10^6 mol $year^{-1}$ km^{-2}. However, large areas of the globe show a marked increase (up to 4×10^6 mol $year^{-1}$ km^{-2}) in HCO_3^- fluxes, especially on exposed continental margins in Indonesia, the English Channel, the Bering Strait, South East China and the Gulf of Mexico. Exposed continental shelves at the LGM and during the early stages of deglaciation (21–11 ka BP) contribute significantly to the global HCO_3^- flux (Table 4). At the LGM, 29% of the total bicarbonate flux is derived from exposed shelf areas, of which 74% came from carbonate regions. The exposed continental shelf areas account for only 13% of the total exposed land at the LGM

Table 2
The breakdown in global land area distribution since the LGM

Age (ka BP)	Exoreic area (10^6 km^2)			Ice sheets (10^6 km^2)
	Total non-glacial	Shelves	Total	
0	102.92	–	102.92	15.61
6	102.39	0.50	102.89	19.94
11	96.82	4.19	101.01	28.42
14	91.26	7.08	98.34	35.39
16	86.67	8.28	94.95	42.25
21	85.64	12.31	97.95	44.94

Table 3
Variation in total non-glacial HCO_3^- flux, and the amount deriving from carbonate rocks and the atmosphere

Age (ka BP)	Flux (10^{12} mol $year^{-1}$)		%HCO_3^- atm
	Total HCO_3^-	HCO_3^- carb.	
0	24.28	8.76	81.96
6	25.03	9.25	81.52
11	28.93	11.79	79.62
14	30.27	13.51	77.68
16	30.56	14.24	76.70
21	30.13	13.88	76.97

(Table 1). Overall, the total HCO_3^- deriving from carbonate weathering ($HCO_{3\ carb}^-$) decreases from 46% at the LGM to 36% at present (Table 5). The highest $HCO_{3\ carb}^-$ flux is at 16 ka BP, which coincides with the peak in total non-glacial, exoreic HCO_3^- flux and a 6% reduction in atmospherically derived HCO_3^-, compared to the present day.

The change in the consumption of atmospheric CO_2 is shown in Table 5. The consumption of atmospheric CO_2 by chemical erosion was ~17% higher during the last glacial maximum than the present day, of which 12 percentage points are derived from increased carbonate weathering and 5 percentage points are derived from silicate weathering. The percentage change in the total consumption of atmospheric CO_2 is similar to that (~20%) calculated by Ludwig et al. (1999), although they calculate that CO_2 consumption due to silicate weathering decreased by ~10%, whereas we calculate that it increased by ~5%. These changes in CO_2 consumption by silicates are small compared to those calculated from the back inversion of marine Ge/Si ratios by Munhoven

Table 4
The proportion of global HCO_3^- and Si fluxes (T mol $year^{-1}$) derived from present-day land and exposed continental shelves throughout the last deglaciation

Age (ka BP)	HCO_3^- (T mol $year^{-1}$)			Si (T mol $year^{-1}$)		
	Main cont.	Shelves	Total	Main cont.	Shelves	Total
0	24.28	–	24.28	5.01	–	5.01
6	24.69	0.34	25.03	5.10	0.03	5.13
11	25.55	3.38	28.93	5.17	0.26	5.43
14	23.75	6.52	30.27	4.87	0.50	5.37
16	22.42	8.14	30.56	4.69	0.61	5.30
21	21.36	8.77	30.13	4.35	0.66	5.00

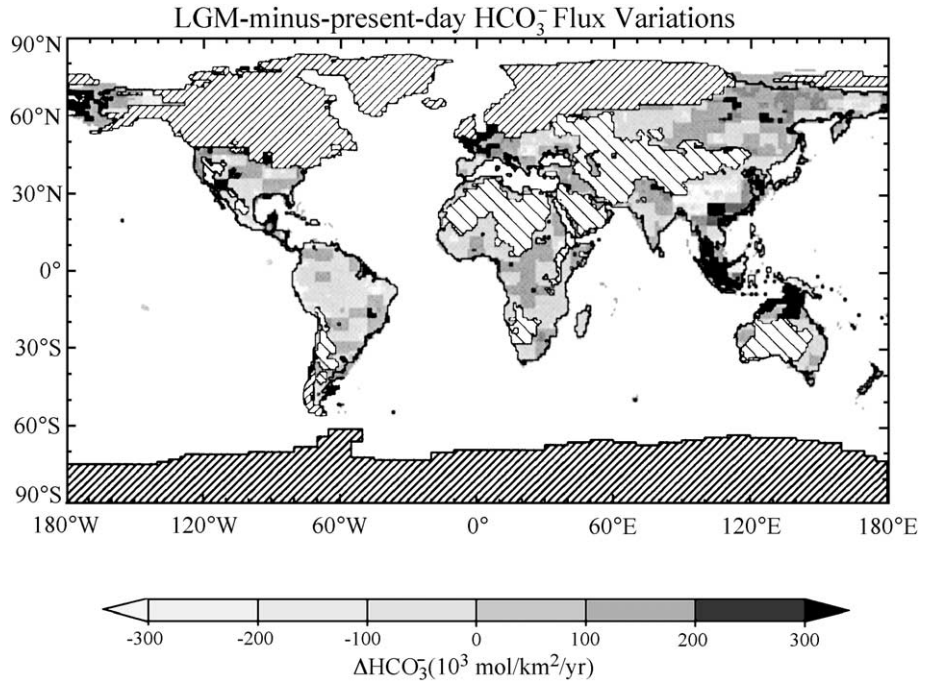

Fig. 5. Differences in the global distribution of HCO_3^- flux between the LGM and present day.

and François (1996), which suggest an increase of ~ 100%. The strong implication is that the marine Ge/Si ratio should carry only a small chemical terrestrial erosion signal on glacial–interglacial timescales, which the following simple modelling approach will demonstrate.

3.3. Si and Ge fluxes: effect on global average riverine Ge/Si

The change in non-glacial Si fluxes over the last deglaciation (Fig. 6) reflects the pattern seen in non-glacial runoff, unlike that of HCO_3^-. The difference between the modelled Si fluxes at the LGM and at the present-day is probably not significant (Table 4).

Table 5
The distribution of the total HCO_3^- flux (T mol year^{-1}) deriving from carbonate lithologies

Age (ka BP)	Main continent	Shelves	Total
0	8.76 (*19.90*)		8.76 (*19.90*)
6	9.00 (*20.19*)	0.25 (*0.22*)	9.25 (*20.41*)
11	9.26 (*20.92*)	2.53 (*2.12*)	11.79 (*23.04*)
14	8.63 (*19.44*)	4.88 (*4.08*)	13.51 (*23.52*)
16	8.08 (*18.38*)	6.16 (*5.06*)	14.24 (*23.44*)
21	7.36 (*17.68*)	6.52 (*5.51*)	13.88 (*23.19*)

The total atmospheric CO_2 consumption rates (T mol year^{-1}) are given in brackets.

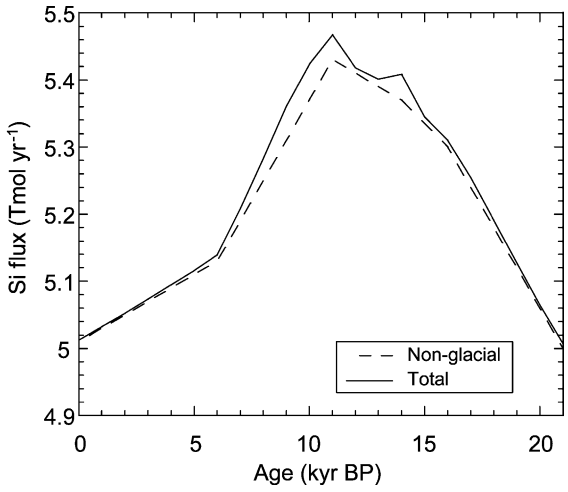

Fig. 6. Variation in the non-glacial and the total (non-glacial + glacial) terrestrial Si flux during the last deglaciation.

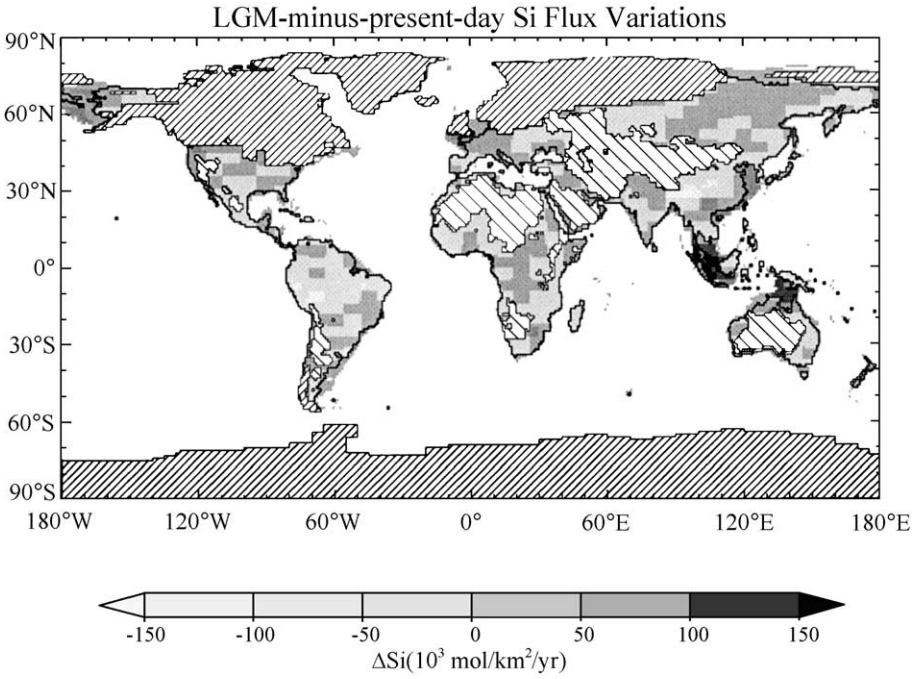

Fig. 7. Differences in the distribution of the global Si flux at the LGM and the present.

During deglaciation, the non-glacial Si flux steadily increases to a maximum of 5.4 T mol year^{-1} at 11 ka BP, before decreasing to its present-day value of 5.0 T mol year^{-1}. Incorporating glacial Si fluxes does not produce a significant increase in the overall Si flux. Indeed, the highest glacial flux of 0.053 T mol year^{-1} occurred at 10 ka BP, increasing the total Si flux by about 1%. Unlike the significant contribution from exposed continental shelves to HCO_3^- fluxes (up to 28%), the influence of these areas is to increase the Si flux by $\sim$ 10%, comparable to the relative increase in land area as a result of exposure of the shelves. However, the highest local increase in Si fluxes do arise from exposed shelves around present-day Indonesia (Fig. 7). The highest fluxes of non-glacial origin at 11 ka BP are a result of increased fluxes on the continents (Table 4). The increase in the continental Si flux between the LGM and 11 ka BP is greater than the decrease resulting from exposed shelf contribution.

The reconstructed non-glacial Ge flux for present day is 3.35×10^6 mol year^{-1} (Fig. 8). This is little different from the calculated non-glacial Ge flux at the LGM, 3.24×10^6 mol year^{-1}. The maximum non-glacial Ge flux was 3.55×10^6 mol year^{-1} at 11 ka BP. The Ge flux is calculated directly from the Si

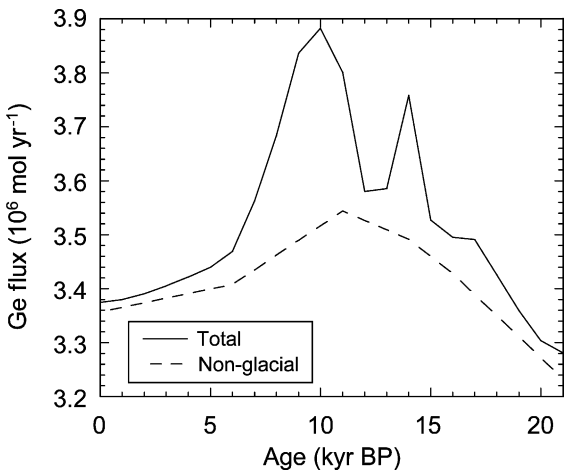

Fig. 8. Variation in the non-glacial and the total (non-glacial + glacial) terrestrial Ge flux during the last deglaciation.

flux and hence the variation of the Ge flux is similar to that of the Si flux over the last deglaciation. Since glacial systems have higher Ge/Si ratios than those of non-glacial systems (Chillrud et al., 1994), the incorporation of the former increases the Ge flux by a maximum of ~10% (at 10 ka BP).

No significant change in Si flux between the present day and the LGM is contrary to previous suggestions that Si fluxes were double at the LGM (Froelich et al., 1992). This proposed doubling of non-glacial Si flux was calculated from Ge/Si ratios derived from ocean cores (Mortlock et al., 1991). The modelled riverine Ge/Si ratio at the LGM (Fig. 9) is only slightly lower than that of present day (0.64 pmol/μmol, compared to 0.66 pmol/μmol) and would not force the marine Ge/Si down to ~0.57 pmol/μmol at the LGM (Fig. 10). However, the steepest increase in the oceanic Ge/Si ratio between 15 and 9 ka BP (Fig. 10) coincides with a marked increase in the global riverine Ge/Si ratio. A simple box model representation of the oceanic Si cycle can be used to evaluate the actual contribution of the glacial and non-glacial fluxes reconstructed here to the observed variations of the marine Ge/Si ratio. If it can be assumed that the accumulation of the opaline remains of diatoms in sea-floor sediments represents the only sink of Si in the ocean, and if fractionation of the seawater Ge/Si ratio by diatoms is negligible, then the

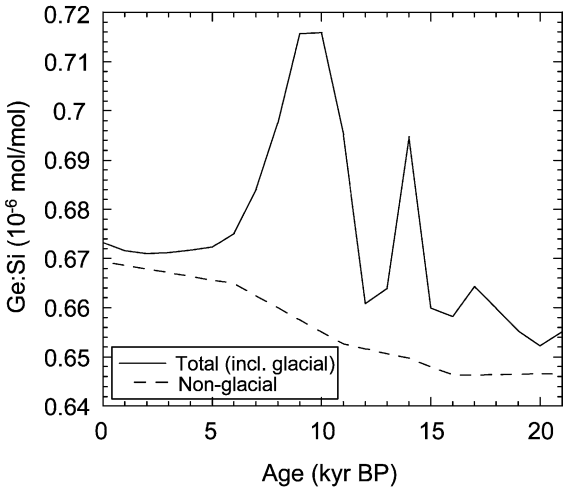

Fig. 9. Variation in the non-glacial and the global (non-glacial + glacial) average riverine Ge/Si ratio over the last deglaciation.

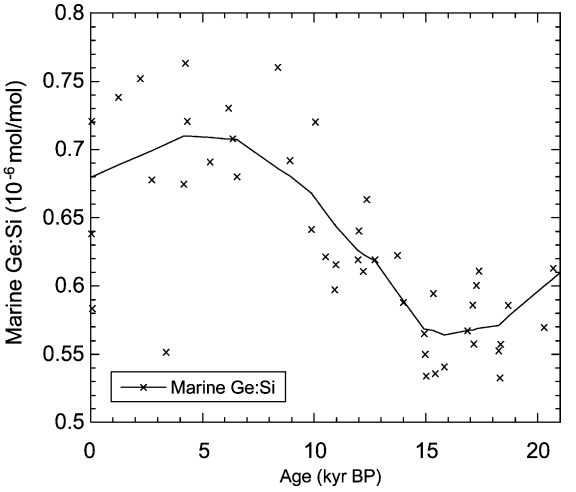

Fig. 10. Variation in marine opaline Ge/Si ratio since the LGM (after Froelich et al., 1992).

evolution of the global average seawater Ge/Si ratio, r, can be written as

$$\frac{dr}{dt} = (r_{\text{riv gl}} - r)\frac{F_{\text{riv gl}}}{Si_{oc}} + (r_{\text{riv ngl}} - r)\frac{F_{\text{riv ngl}}}{Si_{oc}} + (r_{\text{other}} - r)\frac{F_{\text{other}}}{Si_{oc}}. \quad (2)$$

In this equation, Si_{oc} is the total Si content of the ocean. $F_{\text{riv gl}}$, $F_{\text{riv ngl}}$ and F_{other} are the Si supply fluxes to the ocean by glacial meltwater, non-glacial rivers and other sources, respectively. $r_{\text{riv gl}}$, $r_{\text{riv ngl}}$ and r_{other} denote the respective average Ge/Si ratios of these three fluxes. Upon integration, Eq. (2) becomes

$$r(t) - r(t_0) = \int_{t_0}^{t} (r_{\text{riv gl}} - r)\frac{F_{\text{riv gl}}}{Si_{oc}}dt + \int_{t_0}^{t} (r_{\text{riv ngl}} - r)\frac{F_{\text{riv ngl}}}{Si_{oc}}dt + \int_{t_0}^{t} (r_{\text{other}} - r)\frac{F_{\text{other}}}{Si_{oc}}dt, \quad (3)$$

t_0 and t being two arbitrary instants in time. The first two integrals on the right-hand side of Eq. (3) represent the net contributions of the glacial and the non-glacial weathering fluxes to the total variation of the seawater Ge/Si ratio. The evolution of all the variables but Si_{oc} in these two integrals are known during the

deglaciation. With $F_{riv} = F_{riv\ gl} + F_{riv\ ngl}$, the quotients under the two integral signs can be rewritten as

$$\frac{F_{riv\ gl}}{Si_{oc}} = \frac{F_{riv\ gl}}{F_{riv}} \frac{F_{riv}}{Si_{oc}} \quad \text{and} \quad \frac{F_{riv\ ngl}}{Si_{oc}} = \frac{F_{riv\ ngl}}{F_{riv}} \frac{F_{riv}}{Si_{oc}}.$$

Using $t_0 = 16$ ka BP (time of the minimum in seawater Ge/Si—see Fig. 10) and t between 15 and 9 ka BP (i.e., during the time interval of the steepest increase of the seawater Ge/Si), it can be assumed that the variations of F_{riv}/Si_{oc} are small compared to those of the other variables. The first integral in Eq. (3) can thus be rewritten as

$$\int_{t_0}^{t} (r_{riv\ gl} - r) \frac{F_{riv\ gl}}{Si_{oc}} dt \cong \frac{F_{riv}}{Si_{oc}} \int_{t_0}^{t} (r_{riv\ gl} - r) \frac{F_{riv\ gl}}{F_{riv}} dt,$$

and similarly for the second integral. The two integrals can be numerically integrated, using the average seawater Ge/Si evolution depicted in Fig. 10 and the respective reconstructed flux and Ge/Si histories, and setting $F_{riv}/Si_{oc} \cong 1/20{,}000\ year^{-1}$ (Broecker and Peng, 1982). It is found that the glacial flux is responsible for about 7–13% of the increase of r throughout the interval between 15 and 9 ka BP. The contribution from the non-glacial weathering flux to the observed increase decreases from more than 40% before 14 ka BP to 20% at 12 ka BP and 10% at 9 ka BP. The combined glacial and non-glacial fluxes are responsible for 20% of the observed 0.1 pmol/μmol variation of the seawater Ge/Si between 16 and 9 ka BP.

3.4. Evolution of atmospheric CO_2 over the last deglaciation

The effect of the reconstructed variations of HCO_3^- (alkalinity) production and atmospheric CO_2 consumption rates on $^{atms}CO_2$ during the last deglaciation were assessed with a global carbon cycle model. Unfortunately, it was impossible to use the actual fluxes calculated above as inputs to that model. The obtained total HCO_3^- flux of 24.82 T mol $year^{-1}$ would have led to a carbonate compensation depth of less than 1000 m in the global ocean. Appropriate HCO_3^- input and CO_2 consumption scenarios had therefore to be constructed on the basis of the fluxes calculated above. They were obtained by adding the modelled differences of the two fluxes during the deglaciation, relative to their modelled present-day values, onto the respective present-day observed values. Present-day values of 36.3 T mol HCO_3^- $year^{-1}$ and 24.0 T mol CO_2 $year^{-1}$ were adopted (Gaillardet et al., 1999). The carbon cycle model requires the forcing scenarios to cover a whole 120 ka period. The present-day (interglacial) values were adopted for 120 ka BP, and the scenarios were completed by linear interpolation between 120 and 21 ka BP. The actual impact of variable terrestrial chemical erosion on $^{atms}CO_2$ was examined in three different simulations.

1. The glacial and non-glacial chemical erosion fluxes were held constant at their average glacial–interglacial values.
2. Glacial chemical erosion was held constant at the average glacial–interglacial value and non-glacial chemical erosion was allowed to vary.
3. Both glacial and non-glacial chemical erosion were allowed to vary.

The results from the three simulations are shown in Fig. 11. The first simulation shows the effect of oceanic processes alone (viz. temperature and salinity variation, basin-to-shelf transfer of carbonate deposition; see Munhoven and François, 1996 for details).

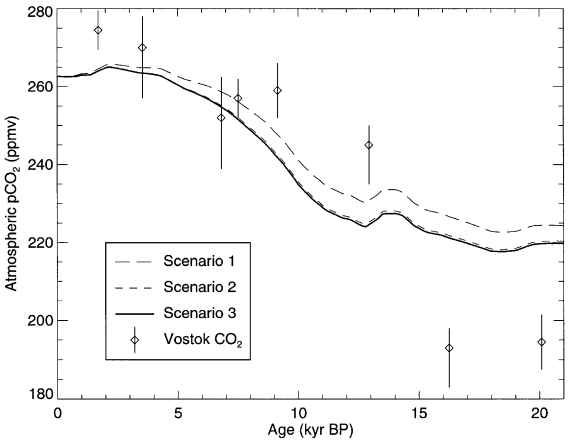

Fig. 11. Modelled variation in atmospheric CO_2 over the last deglaciation as a result of the different model scenarios (see main text). The variation in atmospheric CO_2 recorded in the Vostok ice core (after Barnola et al., 1987) is also included for comparative purposes.

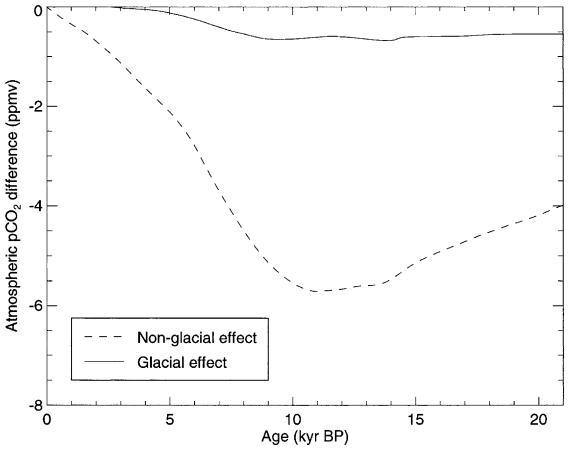

Fig. 12. The effect of variations in glacial and non-glacial terrestrial chemical erosion on atmospheric CO_2 concentrations over the last deglaciation.

Simulation 2 adds the impact of variable *non-glacial* chemical erosion fluxes alone, the impact of which accounts for the difference between Simulations 2 and 1 (Fig. 12). Simulation 3 further includes the effect of variable *glacial* chemical erosion, the impact of which accounts for the difference between Simulations 3 and 2 (Fig. 12). It is apparent that non-glacial chemical erosion has the more pronounced impact on atmospheric CO_2, giving rise to a reduction of ~ 5 ppm at 11 ka BP (Fig. 12). The contribution of glacial chemical erosion is smaller in comparison, being < 1 ppm throughout the last 21 ka BP (Fig. 12). Our predictions for the change in atmospheric CO_2 are comparable to those derived from the Vostok ice core (Barnola et al., 1987) after 9 ka BP. However, the model predicts a greater reduction in CO_2 between 9 and 14 ka BP. At the LGM, $^{atms}CO_2$ was about 190–200 ppm (Barnola et al., 1987). However, the modelled $^{atms}CO_2$ is too high at 225 ppm for the LGM and strengthens the notion that other, significantly important, forcing factors on $^{atms}CO_2$ have not been accounted for in our modelling.

4. Conclusions

Modelling of the variation in terrestrial chemical erosion during the last deglaciation, which includes the effects of runoff enhancement during the disintegration of the Great Ice Sheets, gives little evidence for causing a pronounced change in $^{atms}CO_2$. Key parameters in this modelling approach are the global distribution of runoff and the equations that link the runoff to the chemical erosion fluxes. The confidence that can be placed in the modelling results largely depends on the confidence that can be placed in the definition of these parameters. Clearly, as our ability to estimate the global distribution of runoff in the past increase, so too will our ability to potentially model chemical erosion fluxes. The same argument applies to the definition of the equations that link runoff to chemical erosion fluxes on a given lithology at a resolution of even $1 \times 1^\circ$ resolution. Major new data needs for this type of modelling approach include how these fluxes may depend on temperature and climatic regime, and how accurate is our understanding of the rate of chemical erosion of the "mixed lithology" class.

It was calculated that terrestrial chemical erosion perturbs $^{atms}CO_2$ by ~ 5.5 ppm at most (in the direction of increasing $^{atms}CO_2$ during deglaciation) or 6.5% of the 85 ppm glacial–interglacial change witnessed by the Vostok ice core record (Barnola et al., 1987). For comparison, the $^{atms}CO_2$ increase during deglaciation that results from the combined effects of the decrease in salinity of the oceans, the change in sea surface temperature and the increase in the terrestrial organic carbon reservoir can be estimated at 8.5 ± 17 ppm. The largest part of the calculated 5.5 ppm perturbation is associated with the reduction of the HCO_3^- flux from the continental shelves as sea level rises. Little variation in the terrestrial Si flux is found, and the glacial contribution to the total flux is minimal. It is possible to perturb the riverine Ge:Si ratio significantly, on the assumption that the glacial Ge:Si ratio is high, but the Ge flux calculated is a factor of about 5 too small to give rise to the observed increase in marine opals (Froelich et al., 1992; Mortlock et al., 1991). It may well be the case that the next generation of ocean carbon cycle models will be able to explore in greater detail the change in dissolved inorganic carbon species at depth that arise from changes in ocean circulation (Broecker, 1995; Dokken and Jansen, 1999). $^{atms}CO_2$ perturbations from changing terrestrial chemical erosion may be amplified as a consequence, since it can be expected that enhanced terrestrial chemical erosion during times of reduced sea level are less well buffered by slower deep water turnover. However, the current position is that

variations in terrestrial chemical erosion during deglaciation have little impact on $^{atms}CO_2$, and Si and Ge fluxes.

Acknowledgements

This work was funded by NERC (GR3/11080) and The Royal Society (574006.G503). G.M. is a research associate with the Belgian National Fund for Scientific Research (F.N.R.S.).

References

Amiotte Suchet, P., 1995. Cycle du carbone, érosion chimique des continents et transferts vers les océans. Sci. Geol., Mem. 97, 156 pp. (in French).

Bareille, G., Labracherie, M., Mortlock, R.A., Maier-Reimer, E., Froelich, P.N., 1998. A test of $(Ge/Si)_{opal}$ as a paleorecorder of $(Ge/Si)_{seawater}$. Geology 26 (2), 179–182.

Barnola, J.-M., Raynaud, D., Korotkevich, Y.S., Lorius, C., 1987. Vostok ice core provides 160,000-year record of atmospheric CO_2. Nature 329, 408–414.

Berger, W.H., 1982. Increase of carbon dioxide in the atmosphere during deglaciation: the coral reef hypothesis. Naturwissenschaften 69, 87–88.

Bird, M.I., Lloyd, J., Farquhar, G.D., 1994. Terrestrial carbon storage at the LGM. Nature 371, 566.

Bluth, G.J.S., Kump, L.R., 1994. Lithologic and climatologic controls of river chemistry. Geochim. Cosmochim. Acta 58 (10), 2341–2359.

Broecker, W.S., 1995. The Glacial World According to Wally, 2nd ed. Eldigio Press, Palisades, NY.

Broecker, W.S., Peng, T.-H., 1982. Tracers in the Sea Lamont-Doherty Geological Observatory of Columbia University, Palisades, NY.

Chillrud, S.N., Pedrozo, F.L., Temporetti, P.F., Planas, H.F., Froelich, P.N., 1994. Chemical weathering of phosphate and germanium in glacial meltwater streams: effects of subglacial pyrite oxidation. Limnol. Oceanogr. 39 (5), 1130–1140.

Cogley, J.G., 1998. GGHYDRO—Global Hydrographic Data, Release 2.2. Trent Climate Note 981, Trent University, Dept. of Geography, Peterborough, Ontario.

Dansgaard, W., Johnsen, S.J., Clausen, H.B., DahlJensen, D., Gundestrup, N.S., Hammer, C.U., Hvidberg, C.S., Steffensen, J.P., Sveinbjörnsdottir, A.E., Jouzel, J., Bond, G., 1993. Evidence for general instability of past climate from a 250-kyr ice-core record. Nature 364, 218–220.

Dokken, T.M., Jansen, E., 1999. Rapid changes in the mechanism of ocean convection during the last glacial period. Nature 401, 458–461.

Filippelli, G.M., Carnahan, J.W., Derry, L.A., Kurtz, A., 2000. Terrestrial paleorecords of Ge/Si cycling derived from lake diatoms. Chem. Geol. 168, 9–26.

Froelich, P.N., Blanc, V., Mortlock, R.A., Chillrud, S.N., Dunstan, W., Udomkit, A., Peng, T.-H., 1992. River fluxes of dissolved silica to the ocean were higher during glacials: Ge/Si in diatoms, rivers, and oceans. Paleoceanography 7 (6), 739–767.

Gaillardet, J., Dupré, B., Louvat, P., Allègre, C.J., 1999. Global silicate weathering and CO_2 consumption rates deduced from the chemistry of large rivers. Chem. Geol. 159, 3–30.

Gibbs, M.T., Kump, L.R., 1994. Global chemical erosion during the last glacial maximum and the present: Sensitivity to changes in lithology and hydrology. Paleoceanography 9 (4), 529–543.

Hammond, D.E., McManus, J., Berelson, W.M., Meredith, C., Klinkhammer, G.P., Coale, K.H., 2000. Diagenetic fractionation of Ge and Si in reducing sediments: the missing Ge sink and a possible mechanism to cause glacial/interglacial variations in oceanic Ge/Si. Geochim. Cosmochim. Acta 64, 2453–2465.

Huybrechts, P., 1990. A 3-D model for the Antarctic ice sheet : a sensitivity study on the glacial–interglacial contrast. Clim. Dyn. 5, 79–92.

Huybrechts, P., Oerlemans, J., 1990. Response of the Antarctic ice sheet to future greenhouse warming. Clim. Dyn. 5, 93–102.

Huybrechts, P., T'siobbel, S., 1995. Thermomechanical modelling of Northern Hemisphere ice sheets with a two-level mass-balance parameterization. Ann. Glaciol. 21, 111–116.

Huybrechts, P., T'siobbel, S., 1997. A three-dimensional climate-ice-sheet model applied to the Last Glacial Maximum. Ann. Glaciol. 25, 333–339.

Huybrechts, P., Letreguilly, A., Reeh, N., 1991. The Greenland ice sheet and greenhouse warming. Palaeogeogr., Palaeoclimatol., Palaeoecol. (Glob. Planet. Change Sect.) 89, 399–412.

Jacobs, S.S., Helmer, H.H., Doake, C.S.M., Jenkins, A., Frolich, R.M., 1992. Melting of ice shelves and the mass balance of Antarctica. J. Glaciol. 38, 375–387.

Jones, I.W., Munhoven, G., Tranter, M., 1999. Comparative fluxes of HCO_3^- and Si from glaciated and non-glaciated terrain during the last deglaciation. In: Tranter, M., Armstrong, R., Brun, E., Jones, G., Sharp, M., Williams, M. (Eds.), Interactions Between the Cryosphere, Climate and Greenhouse Gases. IAHS, Wallingford, pp. 267–272.

King, S.L., Froelich, P.N., Jahnke, R.A., 2000. Early diagenesis of germanium in sediments of the Antarctic South Atlantic: in search of the missing Ge sink. Geochim. Cosmochim. Acta 64, 1375–1390.

Kleypas, J.A., Buddemeier, R.W., Archer, D., Gattuso, J.-P., Langdon, C., Opdyke, B.N., 1999. Geochemical consequences of increased atmospheric carbon dioxide on coral reefs. Science 284, 118–120.

Kump, L.R., Alley, R.B., 1994. Global chemical weathering on glacial time scales. In: National Research Council, Panel on Global Surficial Geofluxes (Eds.), Material Fluxes on the Surface of the Earth. National Academy Press, Washington, DC, pp. 46–60.

Kutzbach J., Behling, P., Selin, R., 1996. CCM1 General Circulation Model output data set. IGBP PAGES/WDC-A for Paleoclimatology Data Contrib. Ser. #96-027, NOAA/NGDC Paleoclimatology Program, Boulder, CO. Archived at ftp://ftp.ngdc.noaa.gov/paleo/gcmoutput/ccm1.

Kutzbach, J.E., Gallimore, R., Harrison, S., Behling, P., Selin, R.,

Opdyke, B.N., 1998. Climate and biome simulations for the past 21,000 years. Quat. Sci. Rev. 17 (6/7), 473–506.

Ludwig, W., Amiotte-Suchet, P., Probst, J.-L., 1999. Enhanced chemical weathering of rocks during the last glacial maximum: a sink for atmospheric CO_2? Chem. Geol. 159 (1–4), 147–161.

Mortlock, R.A., Froelich, P.N., 1987. Continental weathering of germanium: Ge/Si in the global river discharge. Geochim. Cosmochim. Acta 51, 2075–2082.

Mortlock, R.A., Charles, C.D., Froelich, P.N., Zibello, M.A., Saltzman, J., Hays, J.D., Burkle, L.H., 1991. Evidence for lower productivity in the Antarctic Ocean during the last glaciation. Nature 351, 220–223.

Munhoven G., 1997. Modelling Glacial–Interglacial Atmospheric CO_2 Variations: The Role of Continetal Weathering. PhD thesis, Université de Liège, Liège.

Munhoven, G., François, L.M., 1994. Glacial–interglacial changes in continental weathering: possible implications for atmospheric CO_2. In: Zahn, R., Pedersen, T.F., Kaminski, M.A., Labeyrie, L. (Eds.), Carbon Cycling in the Glacial Ocean: Constraints on the Ocean's Role in Global Change. Springer-Verlag, Berlin, pp. 39–58.

Munhoven, G., François, L.M., 1996. Glacial–interglacial variability of atmospheric CO_2 due to changing continental silicate rock weathering: A model study. J. Geophys. Res. 101 (D16), 21423–21437.

Murnane, R.J., Stallard, R.F., 1990. Germanium and silicon in rivers of the Orinoco drainage basin. Nature 344, 749–752.

Opdyke, B.N., Walker, J.C.G., 1992. Return of the coral reef hypothesis: basin to shelf partitioning of $CaCO_3$ and its effect on atmospheric CO_2. Geology 20, 733–736.

Peltier, W.R., 1994. Ice age paleotopography. Science 265, 195–201.

Petit, J.-R., Jouzel, J., Raynaud, D., Barkov, N.I., Barnola, J.-M., Basile, I., Bender, M., Chappellaz, J., Davis, M., Delaygue, G., Delmotte, M., Kotlyakov, V.M., Legrand, M., Lipenkov, V.Y., Lorius, C., Pépin, L., Ritz, C., Saltzman, E., Stievenard, M., 1999. Climate and atmospheric history of the past 420,000 years from the Vostok ice core, Antarctica. Nature 399, 429–436.

Reeh, N., 1989. Parameterization of melt rate and surface temperature on the Greenland ice sheet. Polarforschung 59, 113–128.

Sanyal, A., Hemming, N.G., Hanson, G.H., Broecker, W.S., 1995. Evidence for a higher pH in the glacial ocean from boron isotopes in foraminifera. Nature 373, 234–236.

Siegenthaler, U., 1993. Modelling the present-day carbon cycle. In: Heimann, M. (Ed.), The Global Carbon Cycle. Springer-Verlag, Berlin, pp. 367–395.

Walker, J.C.G., Opdyke, B.N., 1995. Influence of variable rates of neritic carbonate deposition on atmospheric carbon dioxide and pelagic sediments. Paleoceanography 10 (3), 415–427.